Bulletin of the Seismological Society of America, Vol. 97, No. 1A, pp. S307–S322, January 2007, doi: 10.1785/0120050632

Rupture Kinematics of the 2005 M_w 8.6 Nias–Simeulue Earthquake from the Joint Inversion of Seismic and Geodetic Data

by A. Ozgun Konca, Vala Hjorleifsdottir, Teh-Ru Alex Song, Jean-Philippe Avouac, Don V. Helmberger, Chen Ji,* Kerry Sieh, Richard Briggs, and Aron Meltzner

Abstract The 2005 M_w 8.6 Nias–Simeulue earthquake was caused by rupture of a portion of the Sunda megathrust offshore northern Sumatra. This event occurred within an array of continuous Global Positioning System (GPS) stations and produced measurable vertical displacement of the fringing coral reefs above the fault rupture. Thus, this earthquake provides a unique opportunity to assess the source characteristics of a megathrust event from the joint analysis of seismic data and near-field static co-seismic displacements. Based on the excitation of the normal mode data and geodetic data we put relatively tight constraints on the seismic moment and the fault dip, where the dip is determined to be 8° to 10° with corresponding moments of 1.24×10^{22} to 1.00×10^{22} N m, respectively. The geodetic constraints on slip distribution help to eliminate the trade-off between rupture velocity and slip kinematics. Source models obtained from the inversion of various combinations of the teleseismic body waves and geodetic data are evaluated by comparing predicted and observed long-period seismic waveforms (100–500 sec). Our results indicate a relatively slow average rupture velocity of 1.5 to 2.5 km/sec and long average rise time of up to 20 sec. The earthquake nucleated between two separate slip patches, one beneath Nias and the other beneath Simeulue Island. The gap between the two patches and the hypocentral location appears to be coincident with a local geological disruption of the forearc. Coseismic slip clearly tapers to zero before it reaches the trench probably because the rupture propagation was inhibited when it reached the accretionary prism. Using the models from joint inversions, we estimate the peak ground velocity on Nias Island to be about 30 cm/sec, an order of magnitude slower than for thrust events in continental areas. This study emphasizes the importance of utilizing multiple datasets in imaging seismic ruptures.

Introduction

The characteristics of large subduction earthquakes—in particular those regarding the rupture kinematics and near-field ground motion—remain poorly known. This is a major societal concern since many of the world's largest cities are situated close to subduction plate boundaries. Because great events have long repeat times, generally hundreds of years, few of them have been recorded by modern geophysical instruments. In addition, along most subduction zones the seismogenic portion of the plate interface lies offshore, making the near-field area inaccessible for direct observation. In the few case studies where geodetic or strong-motion data can be compared with far-field seismological data, it appears that shaking was less severe than in earthquakes of similar magnitude in other tectonic settings. Specific examples include the 1985 M_w 8.1 Michoacan earthquake offshore Mexico (Anderson *et al.*, 1986), the 2003 M_w 8.1 Tokachi-oki earthquake offshore Hokkaido (Honda *et al.*, 2004), and the 1995 M_w 8.1 Antofagasta earthquake offshore Chile (Ruegg *et al.*, 1996). It is, however, unclear whether relatively moderate shaking is a general characteristic of subduction events and whether it is related to propagation effects, to the radiation pattern, or to other source characteristics. The recent 2005 M_w 8.6 Nias–Simeulue earthquake (Fig. 1) is unique in that (1) it occurred within an array of continuously recording Global Positioning System (GPS) stations, the Sumatran GPS Array (SuGAr), and (2) several islands lying above the seismogenic rupture made it possible to measure vertical displacements from the uplift or subsidence of fringing coral reefs (Briggs *et al.*, 2006). These datasets provide excellent constraints on the distribution and magnitude of slip and

*Present address: Department of Geological Sciences, University of California, Santa Barbara, California 93106.

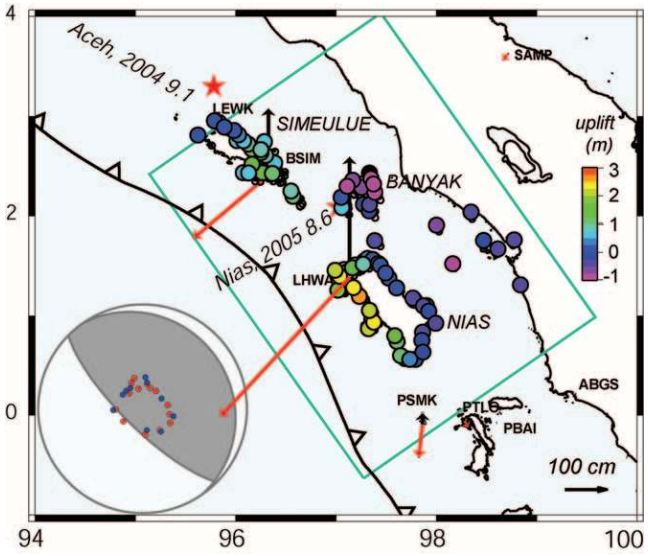

Figure 1. Location of the Nias earthquake. The hypocenters of the 2004 Aceh–Andaman earthquake and 2005 Nias earthquake are show with red stars. The surface projection of the fault plane is demonstrated by the blue rectangle. The vertical component cGPS data displacements are shown in black, and the horizontals are shown in red. Each coral measurement point is shown with a black circle filled with a color scaled with the measured uplift or subsidence. The Simeulue, Nias, and Banyak islands are also shown for reference. The stations used in joint inversions are shown on the beach ball (red for *P* waves and blue for *SH* waves)

make the determination of a more reliable rupture history possible.

Various combinations of teleseismic waveforms and the geodetic dataset are used here to derive a finite source model of the earthquake and to assess their corresponding strong ground motions. Seismic waveforms can be used on their own to invert for fault-slip histories (Ammon *et al.*, 2005), but such modeling is generally nonunique, due to trade-offs between rise time (time for static offsets to develop), slip magnitude, and rupture velocity. The availability of near-field geodetic data significantly reduces these trade-offs. The above source models are tested against long-period data and normal mode excitations, utilizing the sensitivity of these datasets to moment of the earthquake and dip of the fault.

Seismological and Geodetic Data Used in Determining Source Models

Azimuth and relative simplicity were the principal criteria for selecting the teleseismic waveforms from the IRIS network (Fig. 1, inset). Simplicity is judged by examining smaller aftershock observations and picking stations with the least number of unidentified phases. The broadband seismograms were bandpass filtered from 0.8 sec (*P* waves) and 2 sec (*SH* waves) to 200 sec. The long-period seismograms were selected between 40° and 100° distance and bandpass filtered from 100 to 500 sec. Normal modes spectrum below 1 mHz (>1000 sec) are generated by Hann tapering 144 hr of time series prior to discrete Fourier transformation.

We use two types of geodetic data, GPS and coral microatoll measurements, to characterize coseismic surface deformation due to the Nias–Simeulue rupture. An array of continuously recording GPS (cGPS) stations, SuGAr, had been deployed in the years and months preceding the Nias–Simeulue earthquake. The stations record at a 120-sec sampling rate, and the data are available from the Caltech Tectonics Observatory web site (www.tectonics.caltech.edu/sumatra/data). These data and those from the cGPS station at Indonesian National Coordinating Agency for Surveys and Mapping site SAMP near Medan along the northeast coast of Sumatra were used to estimate the coseismic displacements (Briggs *et al.*, 2006). Two GPS stations on Nias (LHWA) and Simeulue Islands (BSIM) recorded large (>2 m) coseismic displacements for the Nias–Simeulue earthquake (Fig. 1). The stations LEWK (to the north) and PTLO and PBAI (to the south) constrain the extent of the rupture in the lateral direction. The GPS coseismic displacements (Briggs *et al.*, 2006) were determined by least-squares fitting the time series from a model consisting of a linear trend for the secular interseismic motion, a heaviside function for the coseismic, an exponential term for postseismic displacement, and sinusoidal terms to correct for annual and semiannual variations (see http://sopac.ucsd.edu for details). The data from the day of the earthquake were discarded. Most of the SUGAR stations in the epicentral area were deployed in January so that the preseismic dataset is limited. The estimates obtained from this approach are consistent with more elaborated models of the postseismic deformation within a few centimeters, showing that the exponential decay law assumed here does not introduce any significant bias (Hsu *et al.*, 2006). In addition, preliminary results from 120-sec solutions show no resolvable postseismic deformation during the first day (S. Owen, personal comm., 2006). Uncertainties are of the order of 0.1–1 cm at the 1σ confidence level. These measurements and their uncertainties are listed in Table 1.

The second geodetic dataset comes from field measurements of coseismic uplift and subsidence (Briggs *et al.*, 2006) utilizing *Porites* coral microatolls, which act as natural recorders of sea level changes with accuracies of a few centimeters (Scoffin and Stoddard, 1978; Taylor *et al.*, 1987; Zachariasen *et al.*, 2000). Coseismic uplift or subsidence can be determined readily from the change in elevation between the preearthquake and postearthquake highest level of survival of living corals with errors of ±6–25 cm. The coral data of Briggs *et al.* (2006) reveal a peak in surface displacement along the west coast of Nias and Simeulue, a trough in displacement between these islands and mainland Sumatra, and a line of no vertical displacement between these two zones of deformation. The measurements were collected about 2 to 3 months after the mainshock and, therefore, in-

clude some amount of postseismic deformation. Modeling of postseismic deformation using the cGPS data (Hsu *et al.*, 2006) predicts vertical postseismic displacements over the first month at the coral measurement points of just a few centimeters. These postseismic displacements are generally about 5% of the measured uplift or subsidence, except at the few points near the down-dip end of the rupture zone. Hence, we assume that a correction for postseismic deformation can be neglected in this study.

The dataset used to derive the source models in this article consist of three-component displacements measured at 16 cGPS stations, 70 measurements of vertical displacement from coral reefs, and 26 seismic records (16 *P* and 10 *SH*) (Fig. 1).

Inversion of Teleseismic Waveforms and Geodetic Data: Modeling Approach

The geodetic data and seismological waveforms were used to determine the finite source model of the rupture parameterized in terms of a grid of point sources. We employed a simulated annealing algorithm to fit the wavelet transform of the seismograms (Ji *et al.* 2002). For the sake of simplicity, we assumed a planar fault plane constrained to meet the Earth's surface at the trench taking into account the ~4-km depth of the trench (Fig. 1). Given the curvature of the trench both along strike and down-dip, this is only a first-order approximation. The dip angle was determined to be 10° based on normal mode excitations and geodetic misfits as discussed below. The geometry of the plane is given in Table 2.

The rupture velocity and the rake angle (80°–115°) vary within given ranges, except for specific cases discussed later. We used 16 km by 16 km subfaults, similar to that used for the Aceh–Andaman earthquake (Ammon *et al.*, 2005, model 3). This grid size was found to offer a good compromise to keep the number of model parameters as low as possible while keeping discretization errors small. We used the hypocenter given by the NEIC (97.013° E, 2.074° N, 30 km). We extracted a one-dimensional (1D) velocity model from the crustal model 3D Crust 2.0 (Bassin *et al.*, 2000) at the epicenter (Table 3).

The displacement field generated by an earthquake can be approximated by summing up the contributions from the various elements (Hartzell and Helmberger, 1982)

$$u(t) = \sum_{j=1}^{n} \sum_{k=1}^{m} D_{jk} \cdot Y_{jk}(\vec{x}, t - d_{jk}/V_{jk}) \cdot \dot{S}_{jk}(t) \quad (1)$$

where j and k are indices of summation along strike and dip, respectively, Y_{jk} are the subfault Green's functions, D_{jk} the

Table 2
Corners of the Planar Fault Geometry

Latitude	Longitude	Depth (km)
−0.63	97.27	3.8
2.42	95.10	3.8
0.98	99.58	59
4.03	97.45	59

Strike, 325°, dip, 10°.

Table 3
Velocity Models Used in the Inversion, Modified from Crust 2.0 at the Location of the Epicenter (97.013° E, 2.074° N)

Depth (km)	v_P (km/sec)	v_S (km/sec)	ρ (kg/m^3)	μ(GPa)
0–1	2.1	1.0	2100	2.1
1–8	6.0	3.4	2700	31.2
8–15	6.6	3.7	2900	39.7
15–22	7.2	4.0	3100	49.6
>22	8.1	4.5	3380	68.5

Table 1
List of Continuous GPS Stations with Coseismic Offsets and Associated 1σ Error Estimates

Station Name	Longitude	Latitude	East (cm)	σ_E (cm)	North	σ_N	Vertical (cm)	σ_Z
ABGS	99.3875	0.2208	−4.54	0.47	−1.17	0.15	−1.48	0.64
BSAT	100.29	−3.08	0.52	0.12	−0.28	0.06	0.00	0.30
BSIM	96.326	2.409	−179.16	0.24	−150.54	0.74	159.59	0.17
LEWK	95.8041	2.9236	−11.30	0.20	6.83	0.45	0.66	0.42
LHWA	97.1345	1.3836	−308.31	0.75	−331.97	0.91	288.11	0.37
LNNG	101.1565	−2.2853	0.55	0.19	−0.50	0.13	−0.99	0.39
MKMK	101.0914	−2.5427	0.54	0.19	−0.44	0.14	−0.52	0.35
MSAI	99.0895	−1.3264	2.03	0.58	−0.48	0.21	−1.42	0.74
NGNG	99.2683	−1.7997	0.85	0.15	−0.67	0.09	−0.96	0.25
PBAI	98.5262	−0.0316	−0.85	0.34	−5.38	0.21	−5.51	0.58
PRKB	100.3996	−2.9666	0.82	0.24	−0.35	0.15	−0.79	0.39
PSKI	100.35	−1.12	0.36	0.20	−0.66	0.09	−0.91	0.22
PSMK	97.8609	−0.0893	−8.87	0.81	−79.00	0.37	26.37	1.04
PTLO	98.28	−0.05	8.22	0.38	−14.95	0.19	−0.59	0.25
UMLH	95.339	5.0531	−3.58	1.58	−5.76	1.40	1.26	1.58
SAMP	98.7147	3.6216	−12.16	0.64	−13.85	0.26	1.33	0.44

dislocations, V_{jk} are the rupture velocities between the hypocenter and subfaults, and d_{jk} are the distance of the subfault from the hypocenter. The rise time for each element is given by $S_{jk}(t)$. Both the V_{jk}s and $S_{jk}(t)$s control the timing of the contribution from each subfault. Thus, the V_{jk}s and $S_{jk}(t)$s are extremely important in estimating strong motions. We approximate the latter as a modified cosine function defined by one parameter, as first proposed by Cotton and Campillo (1995). This greatly reduces the number of parameters compared to the multiple time window used by most researchers (see Ji *et al.* [2002] for a discussion of this issue). The static displacements are calculated with the method developed by Xie and Yao (1989) using the same layered elastic half-space (Table 3) as for the modeling of the seismic waves.

Determination of Seismic Moment and Fault-Dip Angle

The long-period excitation of a point source depends on the source depth, fault geometry, and the seismic moment (Kanamori and Stewart, 1976). In the case of a shallow-dipping thrust fault, the amplitude of excitation is proportional to $M_0 \sin 2\delta$, where M_0 is the moment and δ is the dip angle (Kanamori and Given, 1981), so that the shallower the dip angle, the larger the inferred moment. Therefore without further constraints, it is not possible to get the dip and moment separately from normal mode excitations. The near-field geodetic data shows an opposite trade-off. The shallower the fault-dip angle, the smaller the moment required for the measured displacements. Therefore, the fault-dip angle can be constrained from adjusting the geometry and moment to fit both normal mode amplitudes and geodetic data.

In practice, for any prescribed dip angle, we constrained the moment to the value required to fit the normal mode amplitudes. Given that the centroid moment tensor (CMT) solution indicates a dip angle of 8° for the east dipping plane, we have tested dip angle values between 8° to 12° (Table 4). In order to accurately compute the very long period normal modes, we take into account the coupling caused by Earth's rotation, ellipticity, and heterogeneities of Earth structure (Park and Gilbert, 1986; Dahlen and Tromp, 1998). Following Park *et al.* (2005) we compute the normal mode spectrum, which includes the three-dimensional (3D) earth model (Ritsema *et al.*, 1999) and a group-coupling scheme (Deuss and Woodhouse, 2001). The result of this exercise is that for a dip angle of 12°, the moment is 8.3×10^{21} N m, for 10° it is 1×10^{22} N m and for an 8° we get 1.24×10^{22} N m. For each assumed dip angle we have computed source models derived from the inversion of the geodetic and teleseismic data. We have compared the quality of the fit to the geodetic data provided by each source model based on the reduced chi-square criteria defined as:

$$\chi_r^2 = \frac{1}{n} \sum_{i=1}^{i=n} \left(\frac{(\mathrm{pred}^i - \mathrm{ob}^i)}{\sigma_i} \right)^2, \quad (2)$$

where n is the number of geodetic data σ_i is the uncertainty associated for the each measurement ob^i, pred^i is the predicted displacement at site i. Our results show that the source model with a dip angle of 12° yields a higher reduced chi-square (~21) compared to dip angle of 8° and 10° (~14). The moment required to fit the normal modes for a dip angle of 12° does not allow slip amplitudes large enough to explain the near-field coseismic displacements. Therefore, the average dip angle has to be less than 12°. The lower bound to the fault dip comes from geometrical considerations. Given the hypocenter of the earthquake, a dip angle of less than 8° would meet the earth surface at a considerable distance from the trench. Since the subducting plate's dip angle usually decreases trenchward, a dip of less than 8° is geometrically not plausible. In this study, we chose to use a dip of 10° and a moment of 1×10^{22} N m. The corresponding fit to the normal mode excitations is shown in Figure 2.

Source Models Obtained from the Inversion of Teleseismic Waveforms and Geodetic Data

Since three different datasets are included into the inversion, we tested various solutions and combinations to understand the constraints provided by each particular dataset (Fig. 3). In the source inversions shown in Figure 3, rupture velocity is allowed to vary from 1.5 km/sec to 2.5 km/sec and rise time for each subfault is between 2 and 32 sec. The rupture velocity range was determined by carefully examining misfits of a variety of rupture velocity solutions and will be discussed subsequently. We also performed joint inversions in which the rupture velocity was fixed to some constant value.

The misfit between the measurement and synthetic waveforms is quantified by the sum of L1 and L2 norms

$$e_1 = \sum_{j=j_{\min}}^{j=jc} W_j \cdot \left(\frac{1}{k_j} \sum_{k}^{k_j} |o_{j,k} - y_{j,k}| + \sqrt{\frac{1}{k_j} \sum (o_{j,k} - y_{j,k})^2} \right), \quad (3)$$

where $o_{j,k}$ and $y_{j,k}$ are the wavelet coefficients of the observed and synthetic seismogram for station k and wavelet index j and w_j is the weight of each wavelet channel (Ji *et al.*, 2002). The errors of waveforms are normalized by dividing the calculated error with the error calculated from a random model. The model obtained from the inversion of only the seismic data (Fig. 3a) yields an error of 0.14. The fit to the waveforms is indeed quite good (Fig. 4a). By contrast, this model provides a very poor fit to the geodetic data (Fig. 5a), while models utilizing both geodetic and seismic data (Fig. 3c,d) fit geodetic data very well (Fig. 5c,d). The misfit to the waveforms does not vary much when the geodetic data are taken into account (Fig. 4b,c) and remains in the 0.15–0.20 range (Table 4).

Table 4
Characteristics of Source Models Discussed in This Study

Dataset	Dip	V_r (km/sec)	Rise Time (sec)	Moment Magnitude	Waveform Misfit†	Geodetic Misfit (χ_r^2)‡
Seismic	10	1.5–2.5	2–32	8.6*	0.14	12684.0
cGPS and corals	10	1.5–2.5	—	8.6*	—	5.21
Seismic, cGPS	10	1.5–2.5	2–32	8.6*	0.17	77.4
Seismic, cGPS, and corals	10	1.5–2.5	2–32	8.6*	0.175	11.8
Seismic, cGPS, and corals	10	1.5	2–32	8.6*	0.232	5.4
Seismic, cGPS, and corals	10	2.0	2–32	8.6*	0.189	12.1
Seismic, cGPS, and corals	10	2.5	2–32	8.6*	0.191	13.3
Seismic, cGPS, and corals	10	3.0	2–32	8.6*	0.204	13.3
Seismic, cGPS, and corals	10	2–2.5	2–32	8.6*	0.175	15.0
Seismic, cGPS, and corals	10	1.5	2–32	8.74	0.182	19.4
Seismic, cGPS, and corals	10	2.0	2–32	8.71	0.171	16.5
Seismic, cGPS, and corals	10	2.5	2–32	8.64	0.183	12.1
Seismic, cGPS, and corals	10	3.0	2–32	8.62	0.202	14.6
Seismic, cGPS, and corals	8	2–2.5	2–32	8.66*	0.174	14.4
Seismic, cGPS, and corals	12	2–2.5	2–32	8.55*	0.181	21.3
Seismic	15	1.5–2.5	2–32	8.8	0.150	12,923.0
cGPS and corals	15	—	—	8.59	—	14.6
Seismic, cGPS, and corals	15	1–3	10	8.64	0.169	18.4

*Moment is constrained to the given value *a priori* in the source inversion.
†The waveform misfits are a combination of L1 and L2 norms (Ji *et al.*, 2002).
‡The fit to the geodetic data is quantified from the reduced chi-square as defined by equation (2).

The geodetic inversion (Fig. 3b) was performed with same smoothness and rake parameters as the seismic and joint inversions. Each geodetic measurement is weighted by the $1/\sigma^2$ error, where σ is the associated uncertainty for each cGPS component or coral measurement point. When only the geodetic data were considered in the inversion, we obtain a reduced chi-square value of 5.2 (Table 3). This misfit larger than unity is due in part to a few points at which the residuals exceed notably the uncertainties on the geodetic measurements. The distribution of residuals show that most residuals are about 2 times the uncertainty but that two GPS stations (BSIM and LHWA), contribute most to the misfit with residuals 5 to 10 times larger than the uncertainties on each component. If these two outliers are removed the reduced chi-square value is close to 3. In fact, the weighted root mean square (rms) on the misfits to the GPS horizontal measurement is about 0.45 cm, while assigned uncertainties are of the order of 0.2 cm, weighted rms on the coral data is about 15 cm, similar to assigned data uncertainties. So either the uncertainties on the some GPS measurements with large displacements were underestimated or the model geometry is too simplistic. Approximating the ruptured fault by a single plane is certainly a poor approximation given the curved shape of the trench in the area and probable down-dip curvature of the plate interface. Because of the lack of detailed geophysical constraints on the fault geometry we hold to that approximation for simplicity.

The comparison of joint inversions (Fig. 3c,d) with the purely seismic and geodetic inversions (Fig. 3a,b) shows that the slip distribution is primarily constrained by the geodetic data. Although the joint inversion models are quite different than the pure teleseismic inversion model in terms of slip distribution, the fit to the waveforms is almost equally good (Fig. 4, Table 4). This result emphasizes the nonuniqueness of the solution when only the teleseismic data is used, and the importance of bringing in near-field geodetic constraints, especially for large megathrust earthquakes. Both joint inversions (Fig. 5c,d) show two high-slip patches beneath Nias and Simeulue islands respectively, with a slip deficiency around the hypocenter. The addition of coral data into the joint inversion provides a better spatial coverage and yields a smoother slip distribution (Fig. 5d) compared to the model derived from the teleseismic and cGPS data (Fig. 5c), which shows slip patches biased by the distribution of GPS stations.

The predicted uplift from these models, along with the coral uplift measurements, are shown in Figure 6. Note that the inversion of teleseismic data alone yields a model which seems inadequate to fit the measured pattern of uplift (Fig. 6a). This model predicts high uplift very close to the trench which is not compatible with the modest tsunami produced by this earthquake. Geodetic and joint inversions (Fig. 6b–d) show that the largest uplift is on the northwest of Nias Island, where the cGPS station LHWA recorded about 3 m of uplift and 4.3 m of horizontal displacement toward the trench (Fig. 1). The models derived using both the cGPS and the coral data (Fig. 6b, d) show a more elongated uplift pattern along western Nias Island, while the model using cGPS and seismic data predicts a more circular pattern centered near LHWA, the GPS station with the highest displacement. This shows that the spatial coverage of the coral uplift data helps resolve the shape of the asperity. Another advantage of implementing the coral data into inversions is to constrain the pivot line cutting through the southeast of Nias Island.

In Figure 7, the rupture velocity is fixed to 1.5, 2, 2.5,

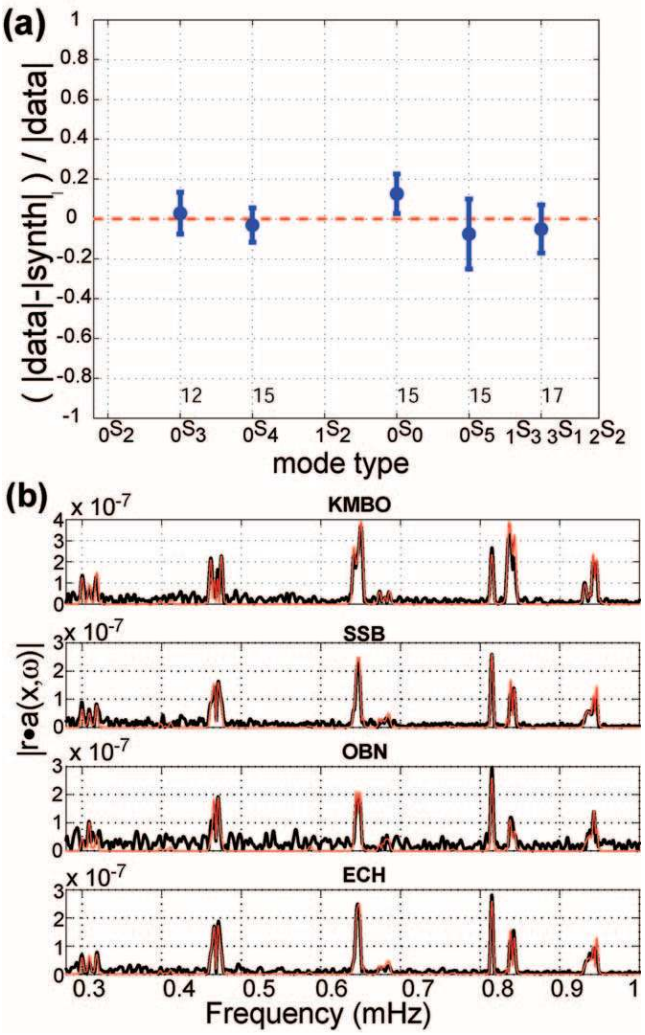

Figure 2. Prediction of Earth's normal modes for a finite fault model using teleseismic and geodetic data with dip angle of 10°, M_w *8.6*, v_r from 1.5 to 2.5 km/sec. (a) Normalized amplitude difference between synthetics and normal mode data, calculated for spheroidal modes ${}_0S_3$, ${}_0S_4$, ${}_0S_0$, ${}_0S_5$, ${}_1S_{3\text{-}3}S_{1\text{-}2}S_2$. Number of stations used to calculate the misfit is given below. Data to noise ratio for ${}_0S_2$ and ${}_1S_2$ are too small to be analyzed extensively. (b) Normal modes spectrum calculated for four stations with good signal-to-noise ratio: KMBO, SSB, OBN, ECH. Synthetics are shown in red and data in black.

and 3 km/sec and the corresponding slip distributions and rise times are shown in panels (a), (b), (c), and (d), respectively. The rise time was allowed to vary from 0 to 32 sec in these inversions. Even with the simple cosine function with one parameter used to characterize the time evolution slip, the model fits the waveform data quite well for a variety of rupture velocities (Fig. 7). We observe a direct trade-off between the rupture velocity and rise time since they are closely linked as indicated by equation (1), especially in the largest asperity under Nias Island. In the model with v_r = 2 km/sec, the rise times *S(t)* are mostly between 10 and 20 sec, whereas in the model with v_r = 3km/sec, rise times are ~25 sec or greater. If the slip amplitudes were not constrained by the near-field geodetic data, the trade-off between rupture velocity and rise times would be more obscure, since slip amplitudes would also be trading-off with these parameters.

The fit to seismic waveforms are slightly better for the case where rupture velocity is fixed to 2 km/sec compared to the cases where it is fixed to some higher or lower value. The fits to the geodetic data on the other hand get better with decreasing rupture velocity (Table 4).

Testing the Source Models against Long-Period Surface Waves

In spite of the constraints provided by the geodetic data, there are still some trade-offs among the model parameters, and we are left with several models that fit the data nearly equally well (Table 4). Since long-period surface waves were not utilized to constrain the inversions, they can be used to constrain further the range of viable models. To account accurately for the 3D structure, ellipticity, gravity, and rotation, we use a spectral element method (SEM) (Komatitsch and Tromp, 2002a, b) to compute synthetic waveforms. We use the 3D crustal model Crust 2.0 (Bassin *et al.*, 2000) and the 3D mantle model s20rts (Ritsema *et al.*, 1999). Each subfault is inserted as a separate source with the mechanism, amplitude, timing, and rise time determined by the source inversions (Tsuboi *et al.*, 2004).

All of the models fit the long periods (100–500 sec) reasonably well (Fig. 8). To quantify the fit, we use the cross-correlation between the data and synthetics in the 400-sec window centered on the Rayleigh waves. Synthetics computed using fixed rupture velocity models have cross-correlation values averaging around 0.97 with better fits in some azimuths. Thus, our models based on relatively short-period teleseismic data and static offsets are very compatible with the seismic data in the 100- to 500-sec-period range.

In the source inversions, the trade-off between the rupture velocity and rise time depends on the apparent velocity of the modeled phase. The apparent velocities of Rayleigh waves are about one third of the *P* waves. As the models with different kinematic parameters were made to fit the *P* and *S* waves, there will be a phase shift of the Rayleigh waves depending on the rupture velocity. If the hypocenter is well located, and correct rupture velocity is used, there should be no time shift between the data and synthetics. Rupture velocities of 2–2.5 km/sec give the least average travel-time shifts relative to the 3D model in order to align the waveforms (Fig. 8 inset).

Strong-Motion Estimates

We use the source models described above to estimate the ground motion in the near field, specifically at the location of the GPS motion LHWA that lies above the largest

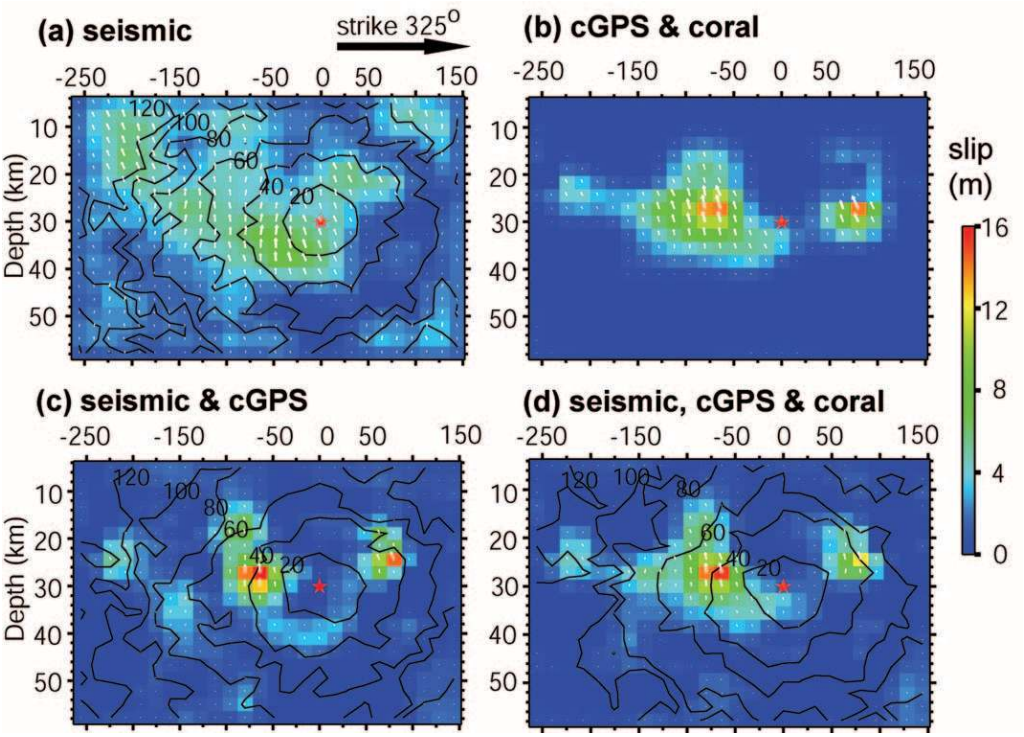

Figure 3. Slip distributions and 20-sec contours of the rupture front for the various source models from the inversion of (a) teleseismic, (b) geodetic (cGPS and coral), (c) teleseismic and cGPS, and (d) teleseismic and all geodetic data. Rupture velocity is allowed to vary between 1.5 and 2.5 km/sec. White arrows show slip vectors for each subfault.

asperity. To obtain detailed information about the rupture process requires near-field seismic data of the type observed for the well-studied 1999 Chi-Chi earthquake. Its strongest motions were recorded near the famous bridge failure, with horizontal offsets of 8 m and uplift of 4.5 m. These offsets occurred in a few seconds and were produced by the nearest small patch of high slip close to the surface. Peak velocities of up to 280 cm/sec were observed and successfully modeled (Ji *et al.*, 2002). For the Nias–Simeulue event we measured 4.5-m horizontal displacement and 2.9-m uplift at the station LHWA, about half of the motion recorded during the Chi-Chi earthquake (Fig. 1).

Prediction of the temporal behavior at this location is displayed for our source models in the frequency range of 1 –5 mHz in Figure 9. The final horizontal displacements in Figure 9a is reached after 60 sec because nearly the entire fault contributes to the final displacement. The vertical displacement is not monotonic because slip in each cell on the megathrust contributes differently to uplift at LHWA. Slip on cells east of the site produce subsidence, while slip on cells west of the site produce uplift. Thus a smaller portion of the fault is responsible for net uplift to sharper offsets and large vertical velocities. The slight difference between the predictions by cGPS-only model and the model that uses both the cGPS and the coral data in Figure 9a is caused by the small difference in location, of the pivot line in the two models. Figure 9b shows the various models calculated with models where rupture velocity is fixed to 1.5, 2, 2.5, and 3 km/sec, respectively. The strong-motion predictions show considerable variation, but all models produce relatively weak strong motions. The largest velocity pulses (~45 cm/sec) are obtained when the rupture velocity is fixed to 3 km/sec; however, this rupture velocity is an extreme upper bound for this earthquake. Figure 9b shows that frequency content of the prediction of ground-motion changes depending on the assumed rupture velocity. This is a result of trade-off the between the rupture velocity and rise time discussed previously. For the higher rupture velocities, the rise times are longer, creating more long-period near-field pulses, and for lower rupture velocities, rise times are shorter, creating local high-frequency data.

Discussion

In this study we attempted to construct a fault-slip model for a great earthquake that explains a wide range of datasets. Each dataset provides key constraints but lacks the individual strength to break the many trade-offs. In this section, we will go over the issues that are investigated in this study and summarize the findings and associated constraints and limitations. For clarity, we have divided this section into four subsections, even though they are all closely related—

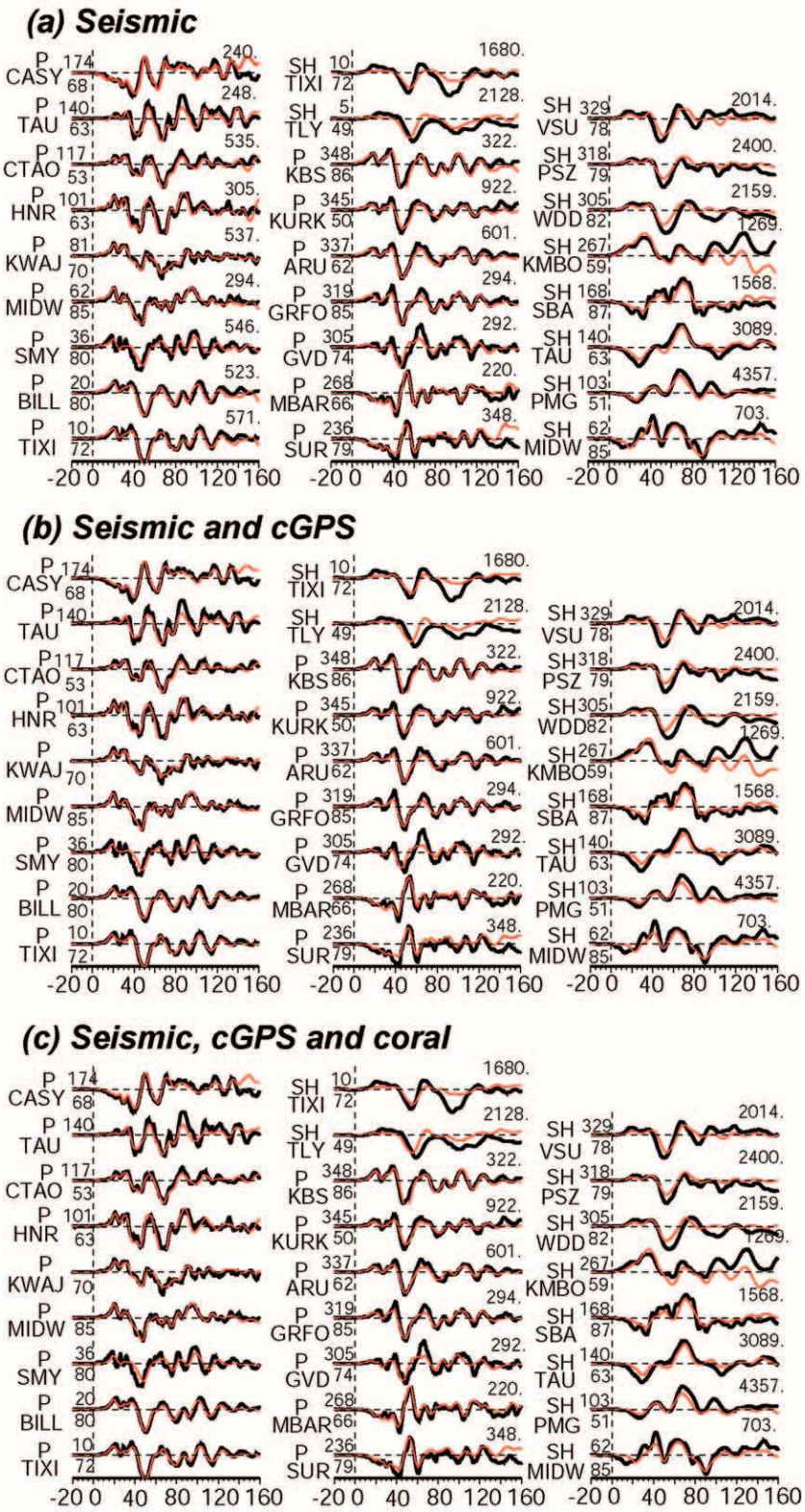

Figure 4. Observed (black) and synthetic (red) teleseismic *P* and *SH* waveforms. Station name, azimuth, and distance are indicated on the left of each trace. The maximum displacement is shown at the top right of each trace in microns. (a) Teleseismic, (b) teleseismic and cGPS, and (c) joint inversion of teleseismic and all geodetic data.

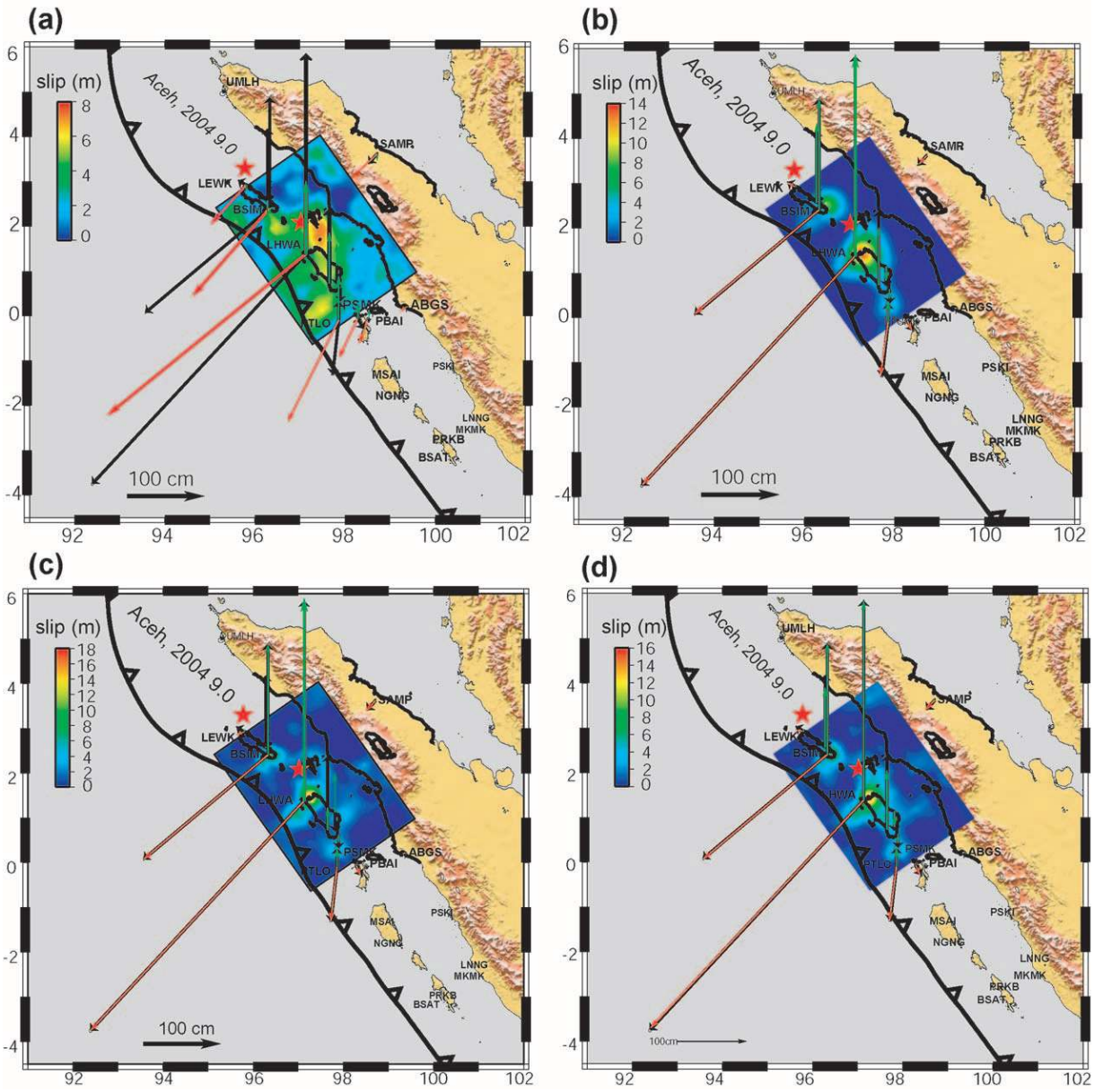

Figure 5. Fits to the 16 cGPS and four coral measurements of uplift for the inversions shown in Figure 3. The slip on the fault is also shown in the maps. The data is in black, the horizontal fits are in red, and vertical fits are shown in gray. (a) Teleseismic, (b) geodetic, (c) teleseismic and cGPS, and (d) joint inversion of teleseismic and all geodetic data

fault geometry, slip distribution, rupture velocity and rise time, and evaluation of near-field strong ground motion.

Fault Geometry

The existence of geodetic data along with normal mode data leads us to estimate the fault-dip angle to be around 8°–10° with corresponding moment magnitudes of 8.66 to 8.60, respectively. However, the amplitude of normal mode excitation depends on the moment and hence on the rigidity structure on the fault. Since we are approximating the subduction zone structure by a 1D velocity model, our estimates of dip angle and moment can be biased. The excitation of long-period seismic waves is even more complex if it is on a structural discontinuity, which is the case for most faults (Woodhouse, 1981).

It should also be noted that fault dip is more likely to increase with depth; therefore, searching for a best-fitting constant dip angle is only a first-order approximation, but it seems a very reasonable assumption in views of the plate interface geometry just north of Simeulue derived from the local monitoring of aftershocks of the 2005 Sumatra earthquake (Araki *et al.*, 2006). In addition, Hsu *et al.* (2006) have explored the influence of the assumed fault geometry,

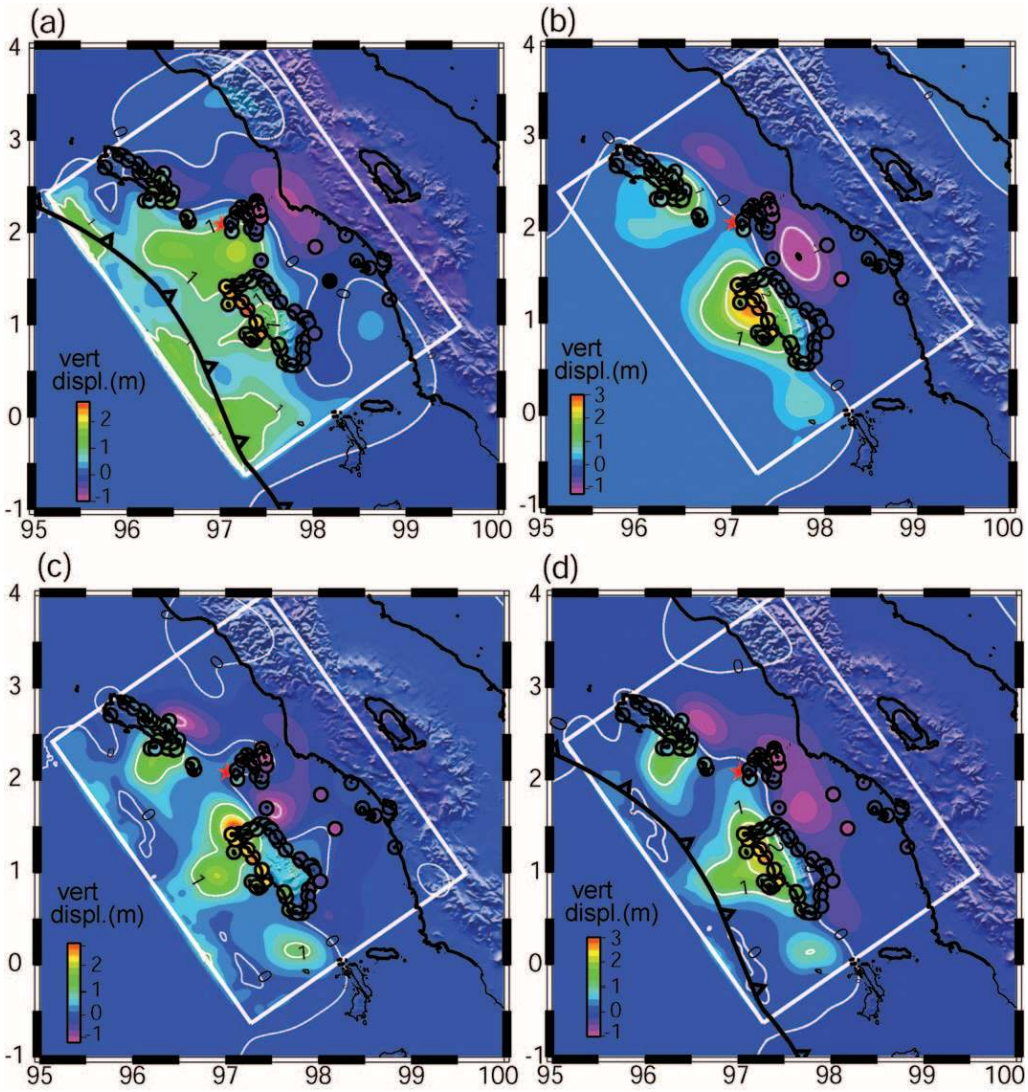

Figure 6. Uplift distribution predicted from the source models obtained from the inversion of (a) teleseismic, (b) geodetic (cGPS and coral), (c) teleseismic and cGPS, and (d) teleseismic and all geodetic data. The measured vertical displacements are also shown in same color scale (circles). Predicted pivot line (line of zero elevation change) is plotted in white and it separates the uplift from the subsidence.

using both curved and planar fault geometries adjusted to the position of the trench and to the aftershock distribution, and found that the sensitivity on the slip distribution is insignificant. A constant dip angle is thus probably a reasonable assumption in this study. Further studies of aftershock relocations using near-field and regional data can help to constrain the velocity structure and geometry of the subduction zone.

Slip Distribution

Our study shows the importance of incorporating geodetic data to predict the slip distribution with accuracy. The comparison of the distribution of uplift predicted from the source model based on the teleseismic data (Fig. 6a) with those predicted from the other source models makes this point clear (Fig. 6c,d). For very large earthquakes like the Nias–Simeulue event, it is a challenge to resolve the slip with only teleseismic data due to trade-offs. Near-field seismograms would prove very valuable to resolve these trade-offs to get a better slip distribution and kinematic parameters with seismology only.

The source models obtained from the joint inversion of the seismological and geodetic data all show that the slip distribution tapers to zero very rapidly up-dip of the slip patches beneath Nias and Simeulue islands. The upward termination of the rupture down-dip of the trench is probably due to inhibition of seismic rupture by the poorly lithified sediments at the toe of the accretionary prism (Byrne *et al.*,

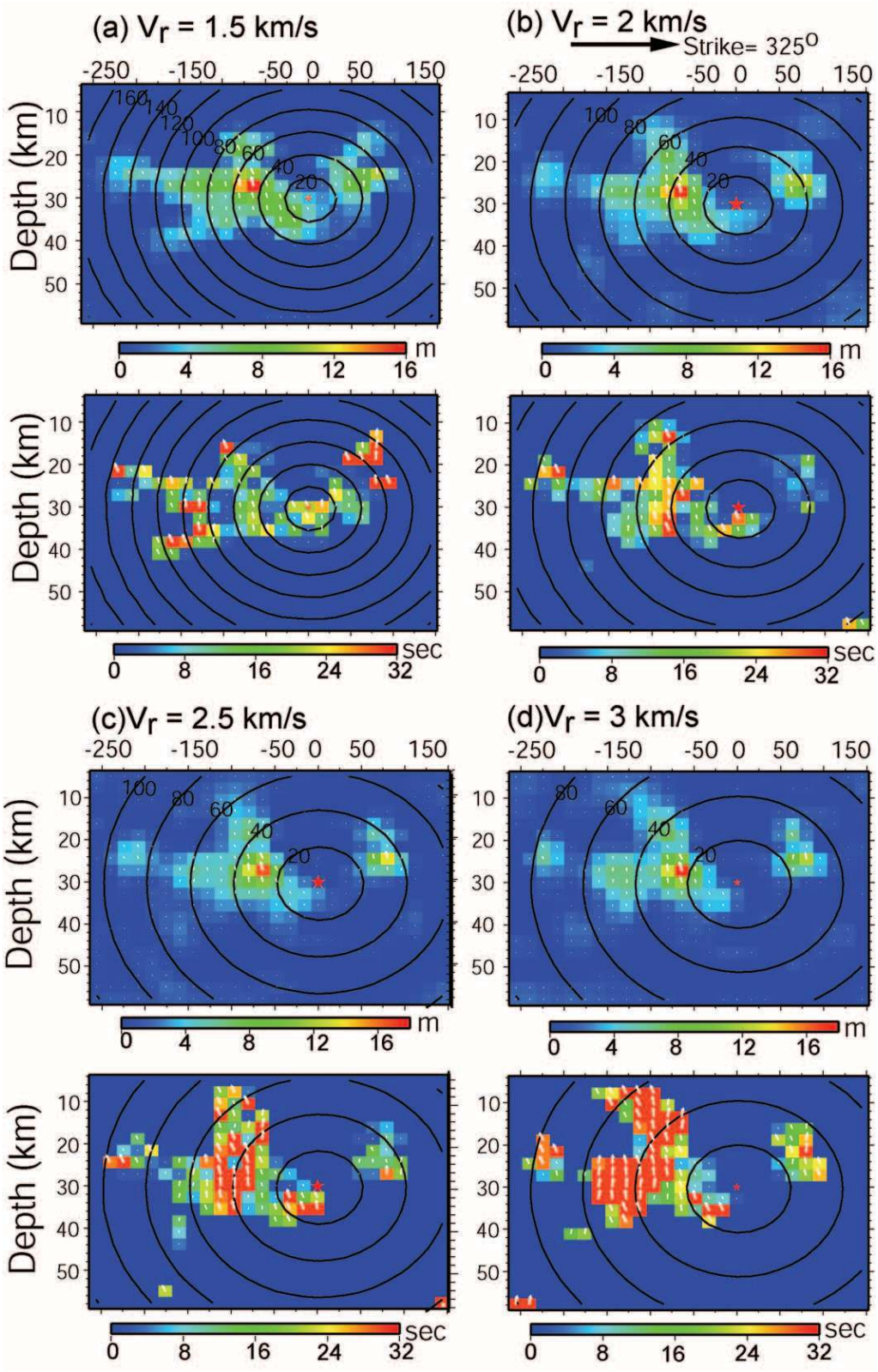

Figure 7. Slip and rise-time distributions on the fault for inversion with (a) v_r = 1.5 km/sec, (b) v_r = 2 km/sec (c) v_r = 2.5 km/sec, and (d) v_r = 3 km/sec. Rise times are shown for the subfaults that slip more then 2 m since the ones that slip less can not be constrained reliably. The rupture front contours are drawn for every 20 sec.

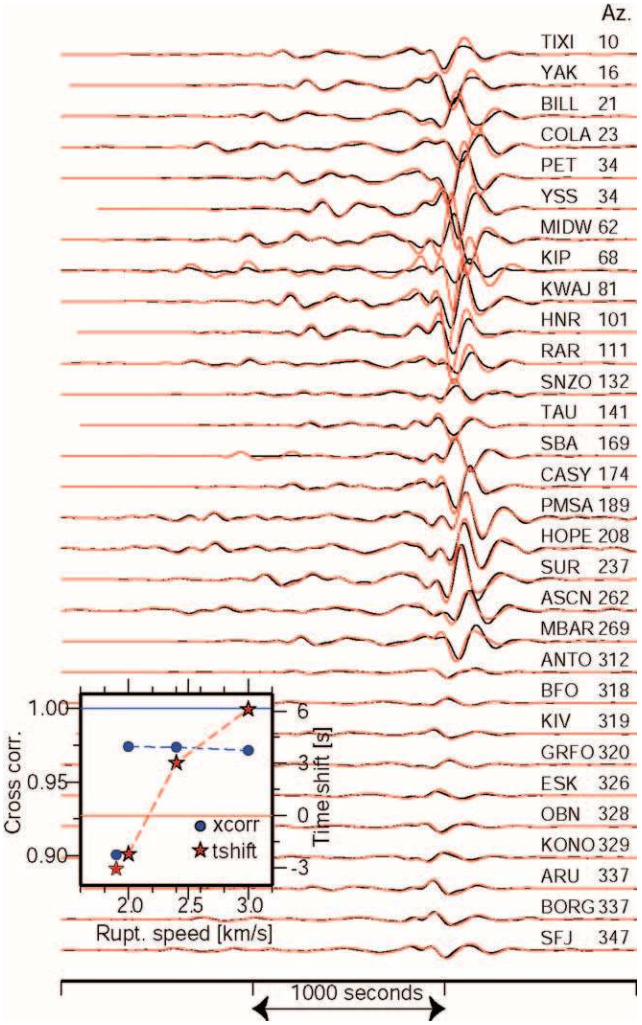

Figure 8. Fits to 100- to 500-sec bandpass-filtered waveform fits computed using a 3D SEM for the model with fixed rupture velocity of 2.5 km/sec (Fig. 7c). The seismograms are 30°–100° distance and are sorted by azimuth and aligned on the Rayleigh wave (3.8 km/sec phase velocity). The inset shows the cross-correlation values (blue circles) and time shifts (red stars) of the Rayleigh waves for the fixed rupture velocity models of 1.5, 2.0, 2.5, and 3.0 km/sec.

1988). Hsu *et al.* (2006) showed that the largest afterslip was observed at the upward termination of the coseismic rupture.

One of the most significant features of the slip pattern is the saddle in slip values between Nias and Simeulue and in the vicinity of the Banyak Islands (Fig. 5). This saddle clearly separates the slip patch to the northwest, near Simeulue island, from that to the southeast, under Nias island. The approximate coincidence of the slip saddle with a major break in the hanging-wall block of the megathrust is intriguing. Karig *et al.* (1980) mapped the Batee fault in this vicinity based on seismic reflection profile, cutting across the forearc from south of the Banyak islands to the northern tip of Nias. They judged the right-lateral strike-slip offset of the continental margin across the fault to be about 90 km. Sieh and Natawidjaja (2000) speculated, on the basis of bathymetric irregularities, that the fault continued in the offshore immediately north of Nias to the trench. Thus, it is plausible that the two principal patches of the 2005 earthquake are separated by a structural break in the forearc. Whether this structure involves the megathrust itself is unknown. But the coincidence of the proposed structure and the division of the 2005 rupture suggests the possibility that the megathrust has a tear or kink between Simeulue and Nias (Briggs *et al.*, 2006). Newcomb and McCann (1987) proposed, on the basis of field and tsunami reports, that the M_w 8.3–8.5 16 February 1861 earthquake rupture extended from the equator to the Banyak Islands. If so, the southern Nias patch of the 2005 earthquake would be a rough repetition of the 1861 rupture. This has not yet been confirmed by paleoseismic work, but if true would provide an interesting contrast to the behavior of the 2005 Nias–Simeulue rupture, which started beneath the Banyak Islands and propagated bilaterally.

Rupture Velocity and Rise Time

Figure 10 summarizes the results that we obtained by varying the rupture velocity in joint inversion source models and the associated (a) geodetic misfit, (b) teleseismic waveform misfit, and (c) Rayleigh-wave cross-correlation time shifts. The geodetic misfit gets lower for the lower rupture velocities. The rupture velocity of 1.5 km/sec actually yields the best fit to the geodetic data (Fig. 10a). Teleseismic data, on the other hand, are best adjusted for the 2 to 2.5 km/sec rupture velocity range (Fig. 10b). Rayleigh-wave time shifts also favor a rupture velocity in the 2–2.5 km/sec range (Fig. 10c). An average rupture velocity of 3 km/sec can be discarded since it does not fit any of the datasets considered. Therefore we conclude that average rupture velocity has to be less than 2.5 km/sec to be consistent with the observations.

The major difference between the slip models with different rupture velocities is that as the rupture velocity is fixed to a lower value, the portion of the fault plane around the hypocenter accumulates more slip. It is the difference in slip amplitudes near the hypocenter that leads to a better fit to the geodetic data for the case of $v_r = 1.5$ km/sec. Hence the observation that the model that best fits to the geodetic data has a slower velocity (1.5 km/sec) than the models adjusted to the seismic data (2-2.5 km/sec) suggests a nonuniform rupture velocity that starts slow at 1.5 km/sec and then accelerates to 2.5 km/sec. Nevertheless the average rupture velocity is in the range of 1.5–2.5 km/sec. Our estimate of rupture velocity is consistent with the average rupture velocity of 2.4 km/sec inferred from the azimuthal variation of *T* waves recorded at Diego Garcia in the Indian Ocean (Guilbert *et al.*, 2005; J. Guilbert, personal comm., 2006). A more detailed modeling of kinematic parameters requires more near-field strong-motion seismograms.

In Figure 10d, we report the average rise time for 1 m of slip as a function of assumed rupture velocity. For the

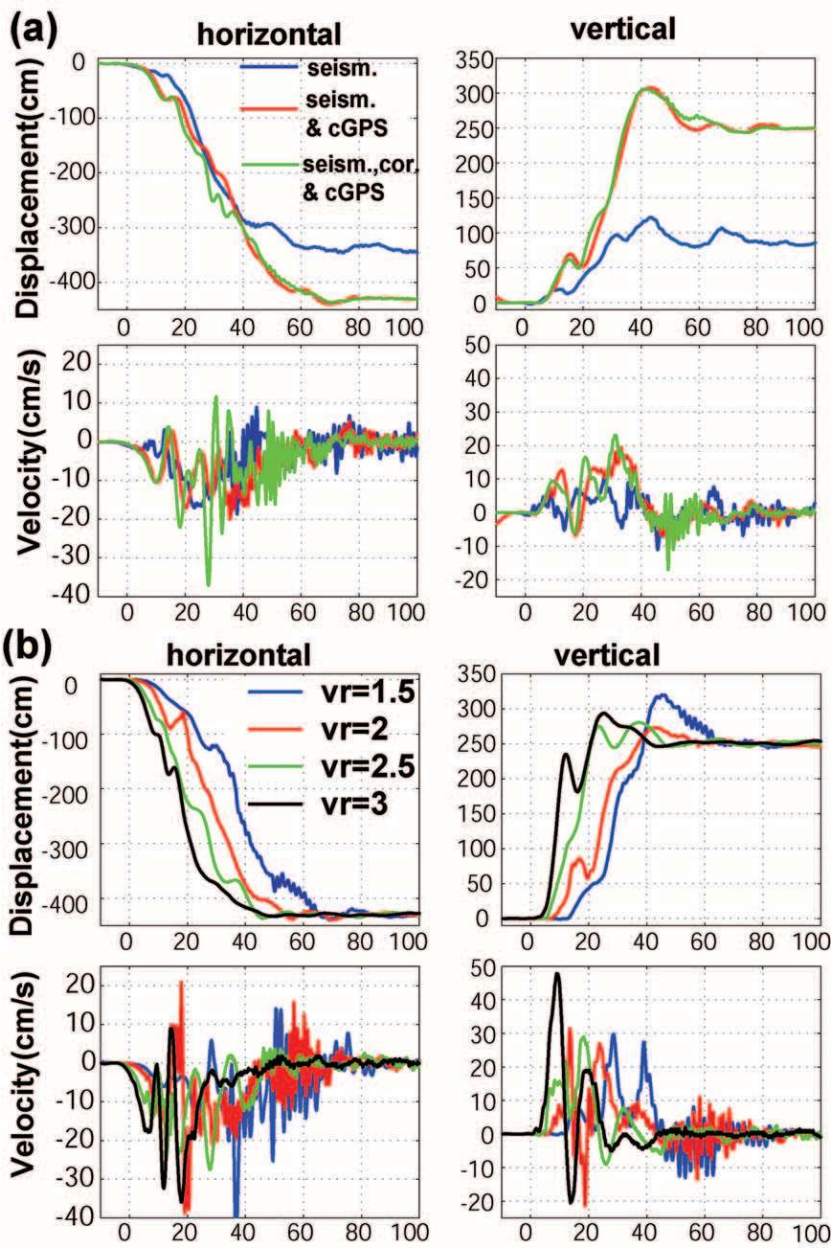

Figure 9. The estimated time evolution of ground displacement and velocity at the station Lahewa (LHWA), Nias Island, for various inversions. (a) Predictions for seismic and joint inversions with GPS and all coral data for rupture velocity varying 1.5–2.5 km/sec., (b) predictions for joint inversions for fixed rupture velocities of 1.5, 2.0, 2.5, and 3.0 km/sec.

plausible range of rupture velocities, this number is of the order of 2–3 s, showing that the rise times associated with this earthquake were relatively long. For the areas that slipped 10 m, the rise time is at least 20 sec. For a comparison, the best observations of strong motions during a large subduction earthquake are for the 2003 M_w 8.1 Tokachi-oki earthquake. The modeling of this earthquake from the near-field strong-motion seismograms shows rise times of about 20 sec and a maximum slip of 7 m for the largest asperity closest to the strong-motion stations (Honda *et al.*, 2004) and about 10 sec on the deeper part of the fault (Yagi, 2004). The rise times are not as well constrained for the 2004 M_w 9.2 Aceh–Andaman earthquake; however, the seismic inversions show that the rise-time functions might be even longer, over 30 sec, for the largest asperity, which slipped 20 m (Ammon *et al.*, 2005). The typical rise times for continental events are generally estimated to be a few seconds (Heaton, 1990). The best constrained continental earthquake is probably the 1999 M_w 7.6 Chi-Chi earthquake, for which abundant geodetic and near-field seismic data exist. The rise times from the largest two asperities of the Chi-Chi earthquake are only about 3 sec (Ji *et al.*, 2003) despite coseismic slip in excess of 12 m, as constrained from GPS and satellite imagery data (Yu *et al.*, 2001; Dominguez *et al.*, 2003). The general observation of long rise times for slip during subduction megathrust earthquakes and rapid rise times during continental earthquakes may reflect a fundamental difference of frictional properties.

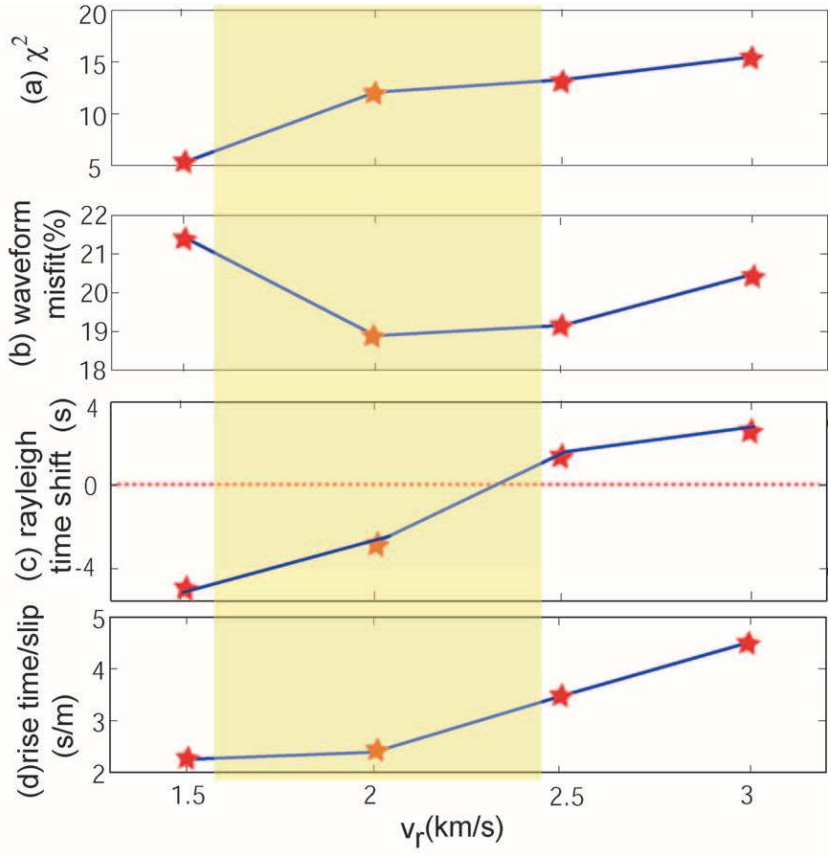

Figure 10. The fits of the fixed rupture velocity joint inversion models to the datasets and the plausible ranges for the dataset. (a) χ^2 misfit to the geodetic data for the various fixed rupture velocity joint inversion models, (b) teleseismic waveform misfit, (c) average Rayleigh wave cross-correlation time shifts in 300- to 500-sec range, and (d) average time consumed for a 1-m slip to occur on the fault. The average value is calculated for all the subfaults that rupture 5 m or more. The plausible range of parameters is shown by the yellow rectangle.

Evaluation of Near-Field Strong Motion

Using the finite source models, we estimate ground motions in the 1–5 mHz frequency band at the GPS site that had the greatest measured ground displacement, LHWA (Fig. 9). Within the bounds of plausible rupture velocities and rise times, maximum particle velocities in the Nias–Simeulue earthquake are between 20 and 30 cm/sec, an order of magnitude lower than for the 1999 Chi-Chi earthquake. These values are compatible with near-field recordings of strong motions from earlier smaller subduction zone events. The peak ground velocity reported from the M_w 8.1 Michoacan earthquake is about 20 cm/sec (Anderson *et al.*, 1986). The highest observed ground velocity, filtered lower than 1 Hz from the Tokachi-oki earthquake is higher: ~66 cm/sec (Yagi, 2004). Most of the stations for the Tokachi-oki earthquake are close to the down-dip end of the rupture, implied by negative vertical displacements on seismograms. Therefore the strongest motions could be higher than the ones recorded. It should be noted that despite the long rise times, the rupture velocity for the Tokachi-Oki earthquake is estimated to be 4.4 km/sec (Yagi, 2004), a much higher value than our estimations for the Nias–Simeulue earthquake, leading to higher observed ground motions. These conflicting results emphasize the importance of rupture velocity in determining the amplitude of the near-field motions in the subduction events.

There are several factors that may have contributed to the relatively low particle velocities during the Nias–Simeulue earthquake. First is the purely geometrical difference between the Nias–Simeulue and Chi-Chi cases. The 6-sec displacement pulse observed on the ground in the Chi-Chi earthquake occurred within a few kilometers from the rupture, whereas the 60-sec displacement at LHWA during the Nias–Simeulue earthquake occurred about 20 km above the megathrust. Thus, the rise time at Chi-Chi was dominated by a small part of the fault immediately adjacent to the station at which the rise time was measured, but the pulse duration at LHWA during the Nias–Simeulue earthquake is an integrates affect of a larger (150 km by 30 km) patch of rupture of the megathrust.

Another reason for the long rise time at LHWA is the low rupture velocity and long rise time on individual cells. If the rupture velocity was about 80% of the shear velocity and also the rise times were similar to Chi-Chi earthquake (~6 sec on the big asperities), the predicted value of the peak particle velocity would reach to 80 cm/sec.

Yet another reason for the slow rise time at LHWA is the radiation pattern and rupture directivity. For crustal strike-slip faults, directivity is known to be a major factor determining the amount and distribution of damage. In subduction zone earthquakes, rupture propagation is commonly toward the trench and along strike. The islands are above the slipping region. Therefore, the islands are not in the di-

rection of the rupture, and consequently experience lower peak ground motions. However, even at the trench, our calculations show weak velocity pulses, since the trench is quite far away from the large offsets. A more detailed study of the strong motions from great subduction earthquakes and their dependence on kinematic parameters requires near-field strong-motion seismograms.

Conclusions

The dip angle and seismic moment of the Nias earthquake is estimated to be 8°–10° with corresponding moments of 1.24×10^{22} to 1.00×10^{22} N m using moment and dip constrains from normal mode data and geodetic misfits. Despite the significant trade-offs between rise time and rupture velocity, the slip pattern of the Nias–Simeulue event is quite well determined, due to the constraints on moment and unique abundance of geodetic data above the source region. Our analysis implies that the earthquake was caused by the rupture of two asperities that did not have significant slip near the trench. A big patch under northern and central Nias island, with maximum slip of about 15 m, a smaller patch under southern Simeulue island, and a slip gap between the two islands are common features of all our joint inversions (Fig. 5). We estimate kinematic parameters by minimizing the time shift in the long-period seismograms and misfit to the dataset used in the inversion. We favor an average rupture velocity of 1.5 to 2.5 km/sec (Fig. 3d). If this is correct, then the rupture velocity is only 50%–60% of the shear-wave speed of the 1D model, far lower than rupture velocities seen during the Chi-Chi and Tokachi-oki earthquakes, for which rupture velocity was typically about 80%–90% of the shear-wave speed. Our modeling yields rise times for the Nias–Simeulue earthquake between 10 and 15 sec, which is similar to other large subduction zone earthquakes.

Acknowledgments

This research was partly funded by the Gordon and Betty Moore Foundation. This is Caltech Tectonic Observatory Contribution Number 38. We appreciate the processing of the SuGAr cGPS data at the Scripps Orbit and Permanent Array Center (SOPAC) by Michael Scharber, Linette Prawirodirdjo, and Yehuda Bock. This manuscript has benefited from helpful suggestions and comments by our reviewers, Roland Burgmann and David Wald.

References

Ammon, C. J., C. Ji, H. K. Thio, D. Robinson, S. Ni, V. Hjorleifsdottir, H. Kanamori, T. Lay, S. Das, D. V. Helmberger, G. Ichinose, J. Polet, and D. Wald (2005). Rupture process of the 2004 Sumatra-Andaman earthquake, *Science* **308,** 5725, 1133–1139.

Anderson, J. G., P. Bodin, J. N. Brune, J. Prince, S. K. Singh, R. Quaas, and M. Onate (1986). Strong Ground Motion from the Michoacan, Mexico, Earthquake, *Science* **233,** 1043–1049.

Araki, E., M. Shinohara, K. Obana, T. Yamada, Y. Kaneda, T. Kanazawa, and K. Suyehiro (2006). Aftershock distribution of the 26 December 2004 Sumatra–Andaman earthquake from ocean bottom seismographic observation, *Earth Planets Space* **58,** no. 2, 113–119.

Bassin, C., G. Laske, and G. Masters (2000). The current limits of resolution for the surface tomography in North America, *EOS* **81,** F897.

Briggs, R. W., K. E. Sieh, A. J. Meltzner, D. H. Natawidjaja, J. Galetzka, B. W. Suwargadi, Y. Hsu, M. Simons, N. D. Hananto, D. Prayudi, and I. Suprihanto (2006). Deformation and slip along the Sunda megathrust in the great 2005 Nias–Simeulue earthquake, *Science* **311,** no. 5769, 1897–1901.

Byrne, D. E., D. M. Davis, and L. R. Sykes (1988). Loci and maximum size of thrust earthquakes and the mechanics of the shallow region of subduction zones, *Tectonics* **7,** 833–857.

Cotton, F., and M. Campillo (1995). Stability of the rake during the 1992, Landers Earthquake—an indication for a small stress release, *Geophys Res. Lett.* **22,** no. 14, 1921–1924.

Dahlen, T., and J. Tromp (1998). *Theoretical Global Seismology*, Princeton University Press, Princeton, N.J.

Dominguez, S., J. P. Avouac, and R. Michel (2003). Horizontal co-seismic deformation of the 1999 Chi-Chi earthquake measured from SPOT satellite images: implications for the seismic cycle along the western foothills of Central Taiwan, *J. Geophys Res.* **108,** doi 10.1029/2001JB000951.

Deuss, A., and J. Woodhouse (2001). Theoretical free-oscillation spectra: the importance of wide-band coupling, *Geophys. J. Int.* **146,** 833–842.

Global Centroid Moment Tensor (CMT) Project catalog search, www.globalcmt.org/CTMsearch.html (last accessed June 2006).

Guilbert, J., J. Vergoz, E. Schissele, A. Roueff, and Y. Cansi (2005). Use of hydroacoustic and seismic arrays to observe rupture propagation and source extent of the M_w = 9.0 Sumatra earthquake, *Geophys. Res. Lett.* **32,** no. 15, L15310.

Hartzell, S., and D. V. Helmberger (1982). Strong-motion modeling of the Imperial-Valley Earthquake, *Bull. Seism. Soc. Am.* **72,** no. 2, 571–596.

Heaton, T. H. (1990). Evidence for and implications of self-healing pulses of slip in earthquake rupture, *Phys. Earth Planet. Interiors* **64,** no. 1, 1–20.

Honda, R., S. Aoi, N. Morikawa, H. Sekiguchi, T. Kunugi, and H. Fujivara (2004). Ground motion and rupture process of the 2004 Mid Niigata Prefecture earthquake obtained from strong motion data of K-NET and KiK-net, *Earth Planets Space* **56,** no. 3, 317–322

Hsu, Y.-J., M. Simons, J-P. Avouac, J. Galetzka, K. Sieh, M. Chlieh, D. Natawidjaja, L. Prawirodirdjo, and Y. Bock (2006). Frictional afterslip following the M_w 8.7, 2005 Nias–Simeulue earthquake, Sumatra, *Science* **312,** 5782, 1921–1926.

Ji, C., D. V. Helmberger, D. J. Wald, and K. F. Ma (2003). Slip history and dynamic implications of the 1999 Chi-Chi, Taiwan, earthquake, *J. Geophys Res.* **108,** no. B9, 2412.

Ji, C., D. J. Wald, and D. V. Helmberger (2002). Source description of the 1999 Hector Mine, California, earthquake, part I: Wavelet domain inversion theory and resolution analysis, *Bull. Seism. Soc. Am.* **92,** no. 4, 1192–1207.

Kanamori, H., and J. H. Given (1981). Use of long-period surface waves for rapid determination of earthquake source parameters, *Phys. Earth Planet. Interiors* **27,** no. 1, 8–31.

Kanamori, H., and G. S. Stewart (1976). Mode of strain release along Gibbs Fracture Zone, Mid-Atlantic Ridge, *Phys. Earth Planet. Interiors* **11,** no. 4, 312–332.

Karig, D. E., M. B. Lawrence, G. F. Moore, and J. R. Curray (1980). Structural framework of the fore-arc basin, NW Sumatra, *J. Geolog. Soc.* **137,** 77–91.

Komatitsch, D., and J. Tromp (2002a). Spectral-element simulations of global seismic wave propagation. I. Validation, *Geophys. J. Int.* **149,** no. 2, 390–412.

Komatitsch, D., and J. Tromp (2002b). Spectral-element simulations of global seismic wave propagation. II. Three-dimensional models, oceans, rotation and self-gravitation, *Geophys. J. Int.* **150,** no. 1, 303–318.

McCaffrey, R., and C. Goldfinger (1995). Forearc deformation and great subduction earthquakes: implications for Cascadia offshore earthquake potential, *Science* **267,** no. 5199, 856–859.

Newcomb, K. R., and W. R. McCann (1987). Seismic history and seismotectonics of the Sunda Arc, *J. Geophys Res.* **92,** no. B1, 421–439.

Park, J., and F. Gilbert (1986). Coupled free oscillations of an aspherical dissipative rotating earth: Galerkin theory, *J. Geophys. Res.* **91,** 7241–7260.

Park, J. T., R. A. Song, J. Tromp, E. Okal, S. Stein, G. Roult, E. Clevede, G. Laske, H. Kanamori, P. Davis, J. Berger, C. Braitenberg, M. V. Camp, X. Lei, H. Sun, H. Xu, and S. Rosat (2005). Earth's free oscillations excited by the 26, December 2004 Sumatra–Andaman earthquake, *Science* **308,** 1139–1144.

Ritsema, J., H. J. van Heijst, and J. H. Woodhouse (1999). Complex shear wave velocity structure imaged beneath Africa and Iceland, *Science* **286,** no. 5446, 1925–1928.

Ruegg, J. C., J. Campos, R. Armijo, S. Barrientos, P. Briole, R. Thiele, M. Arancibia, J. Canuta, T. Duquesnoy, M. Chang, D. Lazo, H. LyonCaen, L. Ortlieb, J. C. Rossignol, and L. Serrurier (1996). The M_w = 8.1 Antofagasta (North Chile) earthquake of July 30, 1995: first results from teleseismic and geodetic data, *Geophys. Res. Lett.* **23,** no. 9, 917–920.

Scoffin, T. P., and D. R. Stoddard (1978). The nature and significance of microatolls, *Philos. Trans. R. Soc. London Ser. B* **284,** 99–122.

Sieh, K., and D. Natawidjaja (2000). Neotectonics of the Sumatran fault, Indonesia, *J. Geophys. Res.* **105,** no. B12, 28,295–28,326.

Taylor, F. W., J. Frohlich, J. Lecolle, and M. Strecker (1987). Analysis of partially emerged corals and reef terraces in the central Vanatu arc: comparison of contemporary coseismic and nonseismic with Quaternary vertical movements, *J. Geophys. Res.* **92,** no. B6, 4905–4933.

Tsuboi, S., D. Komatitsch, C. Ji, and J. Tromp (2004). Broadband modeling of the 2002 Denali fault earthquake on the Earth Simulator, *Phys. Earth Planet. Intenors* **139,** no. 3–4, 305–312.

Woodhouse, J. (1981). The excitation of long period seismic waves by a source spanning a structural discontinuity, *Geophys. Res. Lett.* **8,** no. 11, 1129–1131.

Xie, X., and Z. Yao (1989). A generalized reflection-transmission coefficient matrix method to calculate static displacement field of a dislocation source in a stratified half-space, *Chin. J. Geophys.* **32,** 191–205.

Yagi, Y. (2004). Source rupture process of the 2003 Tokachi-oki earthquake determined by joint inversion of teleseismic body wave and strong ground motion data, *Earth Planets Space* **56,** no. 3, 311–326.

Yu, S. B., L. C. Kuo, Y. J. Hsu, H. H. Su, C. C. Liu, C. S. Hou, J. F. Lee, T. C. Lai, C. C. Liu, C. L. Liu, T. F. Tseng, C. S. Tsai, and T. C. Shin (2001). Preseismic deformation and coseismic displacements associated with the 1999 Chi-Chi, Taiwan, earthquake, *Bull. Seism. Soc. Am.* **91,** 995–1012.

Zachariasen, J., K. Sieh, F. W. Taylor, and S. Hantoro (2000). Modern vertical deformation above the Sumatran subduction zone: paleogeodetic insights from coral microatolls, *Bull. Seism. Soc. Am.* **90,** no. 4, 897–913.

Tectonics Observatory
Division of Geological and Planetary Sciences
California Institute of Technology
Pasadena, California 91125

Manuscript received 13 February 2006.